



# COMMUNICATIONS PHYSICS

## ARTICLE

<https://doi.org/10.1038/s42005-019-0264-z>

OPEN

## Coherent control of magnon radiative damping with local photon states

Bimu Yao<sup>1,2,3</sup>, Tao Yu<sup>4\*</sup>, Y.S. Gui<sup>2</sup>, J.W. Rao<sup>1,2</sup>, Y.T. Zhao<sup>2</sup>, W. Lu<sup>1\*</sup> & C.-M. Hu<sup>2\*</sup>

A magnon, the collective excitation of ordered spins, can spontaneously radiate a travelling photon to an open system when decaying to the ground state. However, in contrast to electric dipoles, magnetic dipoles by magnons are more isolated from the environment, limiting their radiation and coherent communication with photons. The recent progresses in strongly coupled magnon-photon system have stimulated the manipulation of magnon radiation via tailoring the photon states. Here, by loading an yttrium iron garnet sphere in a one-dimensional waveguide cavity supporting both the travelling and standing photon modes, we demonstrate a significant magnon radiative damping that is proportional to the local density of photon states (LDOS). By modulating the magnitude and/or polarization of LDOS, we can flexibly tune the photon emission and magnon radiative damping. Our findings provide a way to manipulate photon emission from magnon radiation, which could help harness angular momentum generation, transfer, and storage in magnonics.

<sup>1</sup>State Key Laboratory of Infrared Physics, Shanghai Institute of Technical Physics, Chinese Academy of Sciences, Shanghai 200083, People's Republic of China. <sup>2</sup>Department of Physics and Astronomy, University of Manitoba, Winnipeg R3T 2N2, Canada. <sup>3</sup>Nantong Academy of Intelligent Sensing, Shanghai Institute of Technical Physics, Chinese Academy of Sciences, Nantong 226000, People's Republic of China. <sup>4</sup>Kavli Institute of NanoScience, Delft University of Technology, 2628 CJ Delft, The Netherlands. \*email: [T.Yu@tudelft.nl](mailto:T.Yu@tudelft.nl); [Luwai@mail.sitp.ac.cn](mailto:Luwai@mail.sitp.ac.cn); [hu@physics.umanitoba.ca](mailto:hu@physics.umanitoba.ca)

**A**magnon is an elementary excitation of magnetic structure that is used as an information carrier in magnonics and magnon spintronics<sup>1–4</sup>, because it carries polarization or “spins” since the magnetization precesses anticlockwise around the equilibrium state<sup>1–4</sup>. The interplay between a magnon and other quasiparticles enriches the functionality of spintronic devices for information transfer with low dissipation. Magnons can excite electron spins by the interfacial exchange interaction (spin pumping)<sup>5,6</sup>, phonons by magnetostriction<sup>7,8</sup>, magnons in a proximity magnet through dipolar or exchange interaction,<sup>9,10</sup> and microwave photons by the Zeeman interaction<sup>11</sup>. The range of spin transport by the electrons and phonons is restricted by their coherence length, which could strongly depend on disorder. Photons are thereby desirable in lifting this constraint due to their long coherence time or length in high-quality optical devices, including cavities and waveguides. Very recently, pioneering works have combined the best features of cavity photons and the long-lifetime magnon in yttrium iron garnet (YIG)<sup>12,13</sup>, demonstrating the cavity-magnon-polariton dynamics<sup>14–19</sup>. Such high-cooperativity hybrid dynamics stimulate the ideas of coherent information processing with magnons. To date, these works have mainly focused on the coherent coupling between the magnon modes and the standing-wave photon modes<sup>14–21</sup> in a confined boundary. However, the efficient delivery of coherent information requires a waveguide supporting the travelling modes<sup>22,23</sup>, in which the magnon radiation in the continuous-wave range<sup>24–26</sup> remains relatively unexplored.

Due to the conservation of angular momentum, a photon emitted by magnon radiation carries a spin current. The accompanying pumping of energy causes magnon radiative damping<sup>24–26</sup>, which reflects the efficiency of these photon emission processes<sup>27–29</sup>. However, weak coupling between the magnetic dipole and the photon makes the control of magnon radiation relatively difficult<sup>27–29</sup>. The magnon-photon interaction is hopefully enhanced by confining the photon modes in a cavity<sup>14–21</sup> or waveguide. This strategy raises the hope of flexibly tuning the magnon lifetime on the basis of intrinsic Gilbert damping. The damping and dephasing rates of magnon in conventional solid-state materials, which are usually difficult to control due to disorder, might result in better controllability from such magnon-photon interactions. Moreover, in information processing the high tunability of photonic environment in a microwave waveguide could improve the pumping efficiency of the photon spin current from magnon radiation<sup>22,23</sup>. We envision that if the mechanism of tuning magnon radiation by local photon states could be demonstrated, various mechanisms that are used to tune photon emission by, for instance, metamaterials, antennas, and superconducting circuits, could be implemented with magnons to add functionality in magnonic applications<sup>27,30–32</sup>.

In this work, we address a general way to control the photon emission from magnons and magnon radiative damping by tuning the local electromagnetic environment. The radiative damping rate is demonstrated to be proportional to the local density of states (LDOS) of photons in a coupled magnon-photon system. We place a YIG sphere into a circular waveguide cavity that resembles to a “clarinet” in shape. Similar to the acoustics of a “clarinet,” standing waves are constructed with the superposition of a continuous-wave background<sup>33,34</sup>, highlighting the crucial differences seen with a confined cavity in a normal coupling scheme. The standing-wave component causes a coherent exchange between magnons and photons and induces a splitting gap in the dispersion, while the superposed travelling-wave component plays the key role of transferring radiated spin information to an open system. By simultaneously involving both standing and continuous waves, magnon radiation

is thereby effectively controlled by photon states and clearly characterized by the magnon linewidth  $\Delta H$  from photon transmission. A relative suppression of the radiative damping at the cavity resonance compared with that at the detuned frequency is observed. This phenomenon seems to be different from the conventional Purcell effect<sup>29,35,36</sup> in the conventional confined cavity, but could be understood by considering open-system photon mode structures. These measurements are well explained as we theoretically establish the relation between macroscopic magnon radiative damping and the microscopic LDOS of microwave photons at a quantitative level. Our result opens opportunities to tune the LDOS involving magnitude and/or polarization to control the photon emission from magnons and magnon radiative damping. To the best of our knowledge, our work is the first convincing observation of LDOS-tunable magnon radiative damping in a coupled magnon-photon system, thus providing the possibility of photon-mediated spin transport with preserved coherence. Due to the linearity nature of our work, we also anticipate that our method offers a general approach to other prototype photonic systems or on-chip integrated devices for advancing the manipulation and delivery of radiated spin information.

## Results

**Construction of photon states.** To clarify the magnon radiative damping controlled by photon states, we first introduce the local electromagnetic environment inside the circular waveguide cavity as shown in Fig. 1a. This waveguide consists of a 16-mm-diameter circular waveguide and two transitions at both ends that are rotated by an angle of  $\theta = 45^\circ$ . The two transitions can smoothly transform the TE<sub>10</sub> mode of a rectangular port to the TE<sub>11</sub> mode of a circular waveguide, and vice versa. Specifically, the microwaves polarized in the  $\hat{x}$ - and  $\hat{x}'$ -directions are totally reflected at the ends of the circular waveguide, forming the standing waves around specific microwave frequencies. In contrast, the microwaves polarized in the  $\hat{y}$ - and  $\hat{y}'$ -directions can travel across the transitions and therefore form a continuum of travelling waves. Therefore, in our device the standing waves can form around particular wave-vectors or frequencies that are superposed on the continuous-wave background<sup>33,34</sup>. The continuous waves help transfer the information to an open system and the standing waves provide the ingredient to form the cavity-magnon polariton. Thus, as opposed to the conventional well-confined cavity with discrete modes, our circular waveguide cavity enables us to add continuous modes to modify the photonic structure<sup>33</sup>.

The modes in our device can be characterized by microwave transmission using a vector network analyzer (VNA) between ports 1 and 2. A standing-wave or “cavity” resonance mode at  $\omega_c/2\pi = 12.14$  GHz is clearly revealed in  $S_{21}$  with a loaded damping factor of  $9 \times 10^{-3}$ , as illustrated by blue circles in Fig. 1b. In the transmission spectrum, the standing waves confined in the waveguide cause a dip in transmission spectrum at the cavity resonance<sup>33</sup>. The travelling continuous waves that deliver photons from ports 1 to 2 contribute a high transmission close to 1. Because continuous waves are not negligible in our device, photon modes cannot be described by a single harmonic oscillator, as shown in previous works<sup>14,16–19</sup>. Hence, the electromagnetic fields in our waveguide cavity are described by a large number of harmonic modes<sup>37–39</sup> over a wide frequency range, and each mode has a certain coupling strength with the magnon mode.

The Fano-Anderson Hamiltonian describes the interaction between the magnon and photon modes as given by Eq. (1)<sup>11,37</sup>:

$$\hat{H}_0/\hbar = \omega_m \hat{m}^\dagger \hat{m} + \sum_{k_z} \omega_{k_z} \hat{a}_{k_z}^\dagger \hat{a}_{k_z} + \sum_{k_z} g_{k_z} (\hat{m}^\dagger \hat{a}_{k_z} + \hat{m} \hat{a}_{k_z}^\dagger), \quad (1)$$

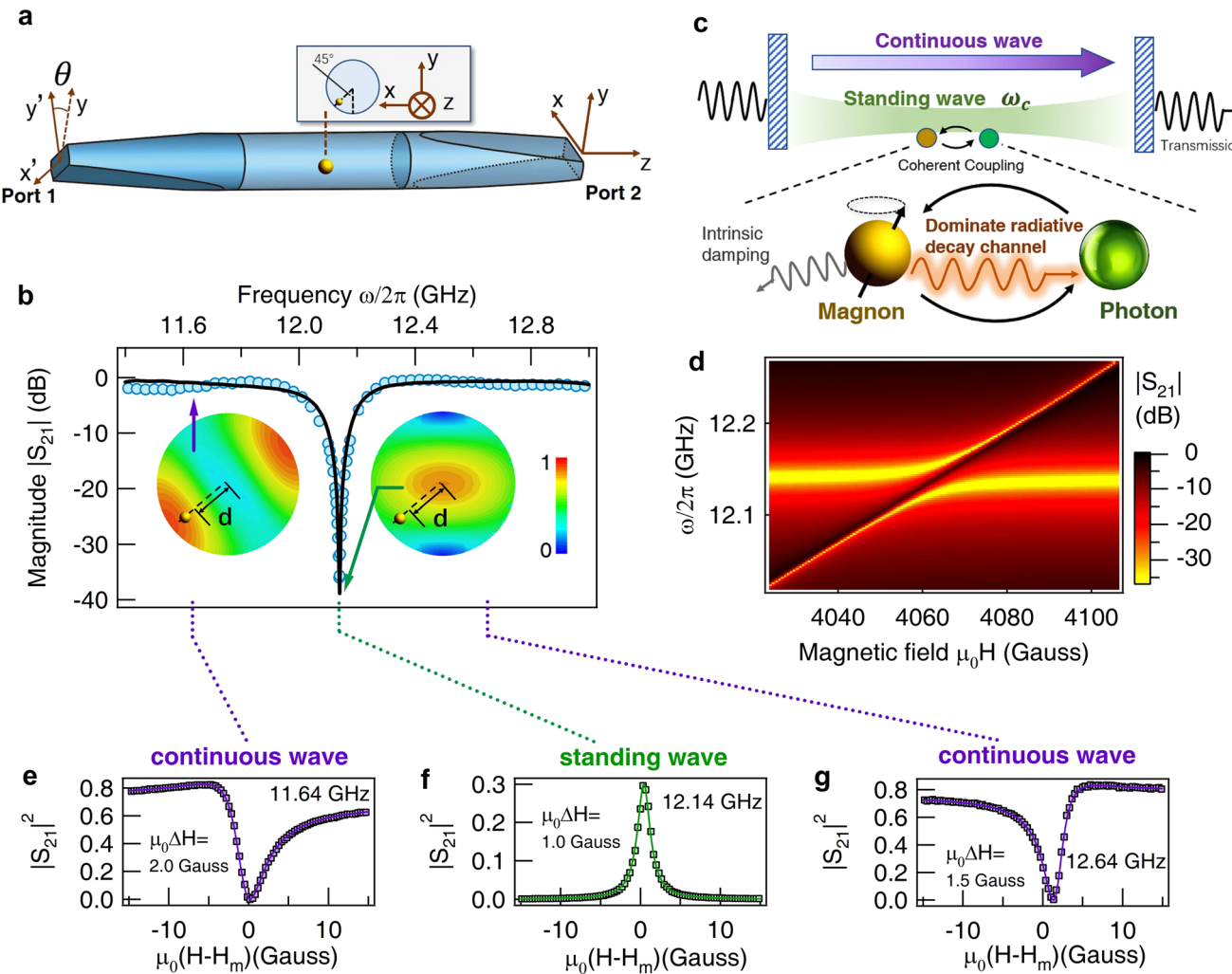


**Fig. 1 Magnon radiative damping controlled by LDOS (local density of photon states).** **a** Experimental setup of the coupled magnon–photon system in a circular waveguide cavity. **b** Transmission coefficient  $|S_{21}|$  from measurement (circles) and simulation (solid lines), with insets showing normalized LDOS distribution for standing-wave resonance at 12.14 GHz and continuous wave at 11.64 GHz. The color bar shows the scale for normalized LDOS with arbitrary unit. **c** By coupling the magnon mode with photon mode in a waveguide cavity, the radiative damping of a magnon can be the dominant energy dissipation channel compared to its intrinsic damping. **d** Measured amplitude of the transmission coefficient  $|S_{21}|$  as a function of the bias magnetic field. Anti-crossing dispersion can be clearly observed for coupled magnon–photon states. The squared amplitudes of the transmission coefficients ( $|S_{21}(H)|^2$ ) are shown at fixed frequencies of 11.64 GHz (**e**), 12.14 GHz (**f**), and 12.64 GHz (**g**), with the x-axis offset  $H_m$  being the biased static magnetic field at magnon resonance. The squares represent the measured  $|S_{21}(H)|^2$  spectra, and the solid line from the lineshape fit represents the reproduced experimental results. In this figure, experimental errors are smaller than the symbol sizes.

where  $\hat{m}^\dagger$  ( $\hat{m}$ ) is the creation (annihilation) operator for the magnon in Kittel mode with frequency  $\omega_m$ ,  $\hat{a}_{k_z}^\dagger$  ( $\hat{a}_{k_z}$ ) denotes the photon operator with wave vector  $k_z$  and frequency  $\omega_{k_z}$ , and  $g_{k_z}$  represents the corresponding coupling strength between the magnon and microwave photon modes. We visualize the magnon Kittel mode as a single harmonic oscillator in Eq. (1). The magnon and photon modes have intrinsic damping originating from an inherent property, but our cavity establishes coherent coupling between them<sup>24–26</sup> as schematically shown in Fig. 1c.

Due to the coherent coupling between the magnon mode and photon mode, the energy of an excited magnon radiates to the photons that travel away from the magnetic sphere. This phenomenon can be pictured as the “auto-ionization” of a magnon into the propagating continuous state that induces the photon emission from the magnon, and hence, there is magnon radiative damping<sup>40,41</sup>. Such “additional” magnon dissipation induced by photon states can be rigorously calculated by the imaginary part of self-energy in the magnon Green’s function,

which is expressed as  $\Delta E_m = \delta_m + \frac{\pi}{\hbar} |\hbar g(\omega)|^2 D(\omega)$ . Here,  $\delta_m$  is the intrinsic dissipation rate of the magnon mode, and  $D(\omega)$  represents the global density of states for the whole cavity that is a count of the number of modes per frequency interval. We note that the above radiative damping is established when the on-shell approximation is valid with the energy shift of the magnon (tens to hundreds of MHz) being much smaller than its frequency (several GHz). By further defining the magnon broadening in terms of magnetic field  $\Delta E = \hbar \gamma \mu_0 \Delta H$ , the magnon linewidth can be expressed as Eq. 2 (Supplementary Note 1)

$$\mu_0 \Delta H = \mu_0 \Delta H_0 + \frac{\alpha \omega}{\gamma} + \frac{2\pi\kappa}{\gamma} R |\rho_l(d, \omega)|, \quad (2)$$

where  $\gamma$  is the modulus of the gyromagnetic ratio, and  $\mu_0$  denotes the vacuum permeability. In Eq. (2), the first two terms represent the linewidth related to inherent damping of the magnon in which  $\mu_0 \Delta H_0$  and  $\alpha \omega / \gamma$  come from the inhomogeneous broadening at zero frequency<sup>42</sup> and the intrinsic Gilbert damping,

respectively. The last term describes the radiative damping induced by photon states in which  $|\rho_l(d, \omega)|$  represents the LDOS of magnetic fields with  $d$  and  $l$  denoting the position and photon polarization direction, respectively. Basically, the LDOS counts both the local magnetic field strength and the number of electromagnetic modes per unit frequency and per unit volume. The coefficient  $\kappa$  is expressed as  $\kappa = \frac{\gamma M_s V_s}{2\hbar c^2}$ , with  $M_s$  and  $V_s$  being the saturated magnetization and volume, respectively, of the loaded YIG sphere. The fitting parameter  $R$  is mainly influenced by cavity design and cable loss in the measurement circuit.

Based on the above theoretical analysis, we find that the radiative damping is exactly proportional to the LDOS  $\rho_l(d, \omega)$ . To observe radiation as a dominant channel for the transfer of magnon angular momentum, both low inherent damping of the magnon and a large tunable  $|\rho_l(d, \omega)|$  are required. In the following experiment, both conditions are satisfied by introducing a YIG sphere with low Gilbert damping, and by modifying the photon mode density through tuning the LDOS magnitude, LDOS polarization, and global cavity geometry.

**Magnon linewidth characterization.** A highly polished YIG sphere with a 1 mm diameter is loaded into the middle plane of a waveguide cavity. Before immersing into the experimental observations, it is instructive to understand the two-dimensional (2D) spatial distribution of the LDOS in the middle plane, which is numerically simulated by CST (computer simulation technology) at the center cross-section that can well reproduce  $|S_{21}|$ , as shown in Fig. 1b. The hot spots for the continuous waves (11.64 GHz) and standing wave (12.14 GHz) are spatially separated, providing the possibility to control LDOS magnitude by tuning the positions of the magnetic sample inside the cavity.

In our first configuration, we focus on the local position with  $d = 6.5$  mm, as marked in Fig. 1b. This position enables the magnon mode not only to overlap<sup>18</sup> with the standing waves but also to couple to the continuous waves. More interestingly, as indicated by the insets in Fig. 1b, the LDOS at  $d = 6.5$  mm is small in quantity at the cavity resonance compared with the ones in the continuous-wave range. This is opposite to the LDOS enhancement at resonance in a conventional well-confined cavity<sup>29,35,36</sup>. Therefore, according to Eq. (2), in contrast to the magnon linewidth enhancement at the cavity resonance in previous works, we expect a different linewidth evolution by varying the frequency, along with a smaller linewidth at cavity resonance  $\omega_c$  compared with that at the detuned frequencies.

Concretely, the magnon linewidth can be measured from the  $|S_{21}|$  spectra in an  $\omega$ - $H$  dispersion map. In our measurement, a static magnetic field  $\mu_0 H$  is applied along the  $\hat{x}$ -direction to tune the magnon mode frequency (close to or away from the cavity resonance), which follows a linear dispersion  $\omega_m = \gamma \mu_0 (H + H_A)$ , with  $\gamma = 2\pi \times 28$  GHz T<sup>-1</sup> and  $\mu_0 H_A = 192$  Gauss as the specific anisotropy field. For our YIG sphere the saturated magnetization is  $\mu_0 M_s = 0.175$  T, and the Gilbert damping  $\alpha$  is measured to be  $4.3 \times 10^{-5}$  by standard waveguide transmission with the fitted inhomogeneous broadening  $\mu_0 \Delta H_0$  equal to 0.19 Gauss. As the magnon resonance  $\omega_m$  is tuned to approach the cavity resonance  $\omega_c$ , a hybrid state is generated with the typical anti-crossing dispersion as displayed in Fig. 1d. A coupling strength of 16 MHz can be found from the Rabi splitting at zero detuning condition, which indicates the coherent energy conversion between the magnon and the photon. This coupling strength is greater than the magnon linewidth but smaller than the cavity linewidth ( $\sim 100$  MHz), suggesting that our system lies in the magnetically induced transparency (MIT) regime rather than the strong coupling regime<sup>18</sup>. Dissipation of the photon

mode allows the delivery of magnon radiation energy to the open environment through the waveguide cavity.

The magnon linewidth (i.e., half-width at half-maximum) is characterized by a lineshape fitting of  $|S_{21}(H)|^2$  that is obtained from the measured transmission at a fixed frequency and different magnetic fields. Here, we focus on  $|S_{21}(H)|^2$  at three different frequencies with one at the cavity resonance  $\omega_c$  and the other two chosen at continuous-wave frequencies above and below  $\omega_c$  (11.64 and 12.64 GHz, respectively). As the photon frequency is tuned from the continuous-wave range to the cavity resonance  $\omega_c/2\pi = 12.14$  GHz, we observe that the lineshape of  $|S_{21}(H)|^2$  varies from asymmetry to symmetry, as shown in Fig. 1e-g. These results can be well fitted (see solid lines in Fig. 1e-g), which helps us to identify an obvious linewidth suppression from the continuous-wave range (2.0/1.5 Gauss) to cavity resonance (1.0 Gauss).

When compared with the magnon linewidth  $\mu_0 \Delta H$  at detuned frequencies, the magnon linewidth shows a relative suppression at the cavity resonance rather than the linewidth enhancement in a conventional coupled magnon–photon system in the cavity<sup>19,43</sup>. Such suppression of the magnon linewidth qualitatively follows the LDOS magnitude, which also shows a decrease in quantity at the cavity resonance. This finding qualitatively agrees with our theoretical expectation from Eq. (2). In the following subsections, it is necessary to study the relationship between linewidth and LDOS at a quantitative level by using both theoretical calculation and experimental verification.

**Magnon radiation controlled by LDOS magnitude.** In this subsection we provide a quantitative control of magnon radiative damping by tuning the LDOS magnitude over a broadband frequency range. The spatial variation of the magnetic field in our waveguide cavity allows us to realize different LDOS spectra simply by choosing different positions. Similar to the experimental settings in the above section with  $d = 6.5$  mm, we display a broadband view of the LDOS for polarization by using simulation illustrated in Fig. 2. Although  $\rho_x(\omega)$  in Fig. 2a shows a typical resonance behavior, its contribution to the magnon radiation is negligible here according to the well-known fact that only photon polarization that is perpendicular to the external static magnetic field  $H$  drives the magnon linear dynamics. By following this consideration, we further simulate  $\rho_\perp = \sqrt{\rho_y^2 + \rho_z^2}$ , which plays a dominant and important role in the magnon–photon interaction as displayed in Fig. 2b.  $\rho_\perp(\omega)$  shows a dip at the cavity resonance with respect to the frequency.

It is clearly seen that due to the enhancement of the global density of states at the mode cut-off of the waveguide, continuous-wave LDOS becomes increasingly significant when the frequency is decreased to approach the cut-off frequency ( $\sim 9.5$  GHz). This phenomenon can be viewed as a Van Hove singularity effect in the density of states for photons (see independent observation via a standard rectangular waveguide in Supplementary Note 2). Because the singularity effect is involved in the coupled magnon–photon dynamics, we can obtain a larger linewidth at the detuned frequency range, which causes a relative linewidth suppression at the cavity resonance. In contrast to the linewidth enhancement from typical Purcell effects in a confined cavity, the results shown in Fig. 2c provide a new linewidth evolution process over a broadband range. These results are obtained from lineshape fitting at each frequency, with the error of fit being smaller than the symbols. Furthermore, to compare with our theoretical model, we perform calculations using Eq. (2) with  $\kappa R = 4.0 \times 10^{22}$  m<sup>3</sup> s<sup>-2</sup>, where the fitting parameter quantity  $R \sim 0.8$ . It can be observed in Fig. 2c that the

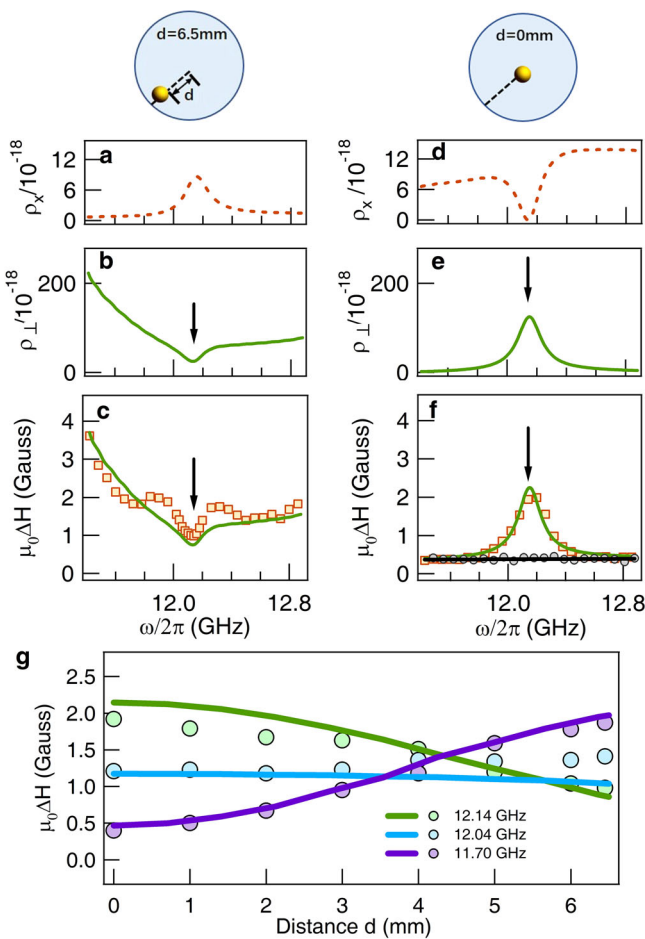


**Fig. 2 LDOS (local density of photon states) magnitude dependence.**

**a, b** Simulated  $x$ -direction LDOS ( $\rho_x$ ) and perpendicular LDOS ( $\rho_\perp$ ) at  $d = 6.5$  mm. **c** Measured linewidth-frequency ( $\mu_0\Delta H - \omega$ ) relation (shown in squares) with calculated lines from the model (green line) at  $d = 6.5$  mm. **d, e** Simulated LDOS  $\rho_x$  and  $\rho_\perp$  at  $d = 0$  mm. **f** Measured linewidth-frequency  $\mu_0\Delta H - \omega$  relation (squares) with calculated lines from the model (green line) at  $d = 0$  mm. Black circles and lines indicate the measured and fitted intrinsic linewidths, respectively. **g** Magnon linewidth  $\mu_0\Delta H$  evolution with tuning positions for different frequencies, with circles and solid lines representing the measured magnon linewidth and the linewidth computed from LDOS, respectively. Errors of linewidth fit are smaller than the size of symbols.

measured  $\mu_0\Delta H$  agrees well with the computed values from our theoretical model. This suggests that the linewidth is coherently controlled by the LDOS magnitude and shows that radiative power emission induced by continuous waves can unambiguously exceed that induced by standing waves.

To create a different LDOS magnitude to tune the magnon radiation, the magnetic sphere is moved to the center of the cross-section with  $d = 0$  mm. The simulated LDOS  $\rho_x$  and  $\rho_\perp$  are illustrated in Fig. 2d, e, respectively. The effective LDOS  $\rho_\perp$  shows an enhancement at the cavity resonance but decreases at the continuous-wave range. Similar to the frequency dependence of the LDOS magnitude, the magnon linewidth is observed to be enhanced at the cavity resonance, but decreased at the continuous-wave range. This relation between the magnon linewidth and LDOS is again quantitatively verified by the good agreement between measurement and calculated results from Eq. (2), as shown in Fig. 2f. In particular, as the continuous-wave LDOS approaches zero, the radiative damping from LDOS thereby becomes negligibly small. In this case, we find that the

magnon linewidth exactly returns to its intrinsic damping  $\mu_0\Delta H_0 + \alpha\omega/\gamma$  measured in an independent standard waveguide.

Finally, at a detailed level, to continuously tune the ratio of the standing/continuous-wave LDOS magnitude, the position of the YIG sphere is moved where  $d$  varies from 0 to 6.5 mm. Typically, for the three different frequency detunings at 0, -100, and -440 MHz, our results in Fig. 2g show that the magnon linewidth can be controlled by the enhancement, suppression, or negligible variation in the position dependence. As shown in Fig. 2g, these results show good agreement with the theoretical calculation, suggesting that the magnon linewidth can be controlled on demand by tuning the LDOS magnitude. Moreover, the photon emission efficiency from the magnon radiation can in principle be significantly enhanced with a larger magnetic sphere and a waveguide with a smaller cross-section. For example, a magnetic sphere with 2-mm diameter and a waveguide with half radius would enhance the radiation rate by 16 times (Supplementary Note 1).

**Magnon radiation controlled by LDOS polarization.** Having shown the relation between the magnon radiative damping in  $\mu_0\Delta H$  and the LDOS magnitude, here we would like to introduce LDOS polarization as a new degree of freedom to control the magnon radiation. In our experiment, by placing the YIG sphere at  $d = 2.3$  mm, the control of effective LDOS polarization  $\rho_\perp$  around the magnetic sphere can be simply achieved by varying the direction of the external static magnetic field  $H$  with a relative angle  $\varphi$  to the  $\hat{x}$ -direction as shown in Fig. 3a. Please note that compared with the complicated operation of varying the position of the YIG sphere inside a cavity, here the LDOS was controlled continuously over a large range simply by rotating the orientation of the static magnetic field. Based on the orthogonal decomposition of the LDOS for photons,  $\rho_\perp$  is simulated for three typical angles, that is,  $\varphi = 0^\circ, 45^\circ$ , and  $90^\circ$ , as shown in Fig. 3b. For the relative angle  $\varphi = 0^\circ$  with  $H$  being exactly in the  $\hat{x}$ -direction, the LDOS is dominated by the standing-wave component, which could provide the largest coupling with the magnon mode at the cavity resonance. As the relative angle  $\varphi$  approaches  $90^\circ$ , continuous waves become increasingly dominant in their contribution to the LDOS, causing a peak-to-dip flip for the LDOS around the resonance frequency  $\omega_c$  in Fig. 3b.

Accordingly, in our experiment, we obtain a magnon linewidth enhancement at  $\varphi = 0^\circ$  as shown in Fig. 3c with red squares. As the relative angle  $\varphi$  is tuned towards  $90^\circ$ , we thereby anticipate and indeed obtain a linewidth suppression at the cavity resonance shown with blue squares, showing good agreement with the linewidth scaling of  $\rho_\perp$  in Eq. (2). The theoretically calculated linewidth  $\mu_0\Delta H$  is plotted for each  $\varphi$  in Fig. 3c with  $\kappa R$  consistent with the previous subsection. The good agreement between experimental and theoretical findings suggests flexible control of magnon radiation via LDOS polarization. Moreover, by not restricting the tuning of the relative angle between  $H$  and LDOS polarization in the 2D plane, there may be an increased possibility of realizing magnon radiation engineering by pointing  $H$  to an arbitrary direction in the whole 3D space.

**Magnon radiation controlled by cavity geometry.** Our device allows us to tune the LDOS magnitude and polarization together simply by rotating the relative angle  $\theta$  between the two transitions<sup>33</sup>, that is, the global geometry of our circular waveguide cavity. This approach can validate and enrich our observations that the same magnon harmonic mode radiates a different amount of power depending on the surrounding photon environment. In this subsection, we insert a rotating part in the middle plane of the cavity, so that the relative angle  $\theta$  between two

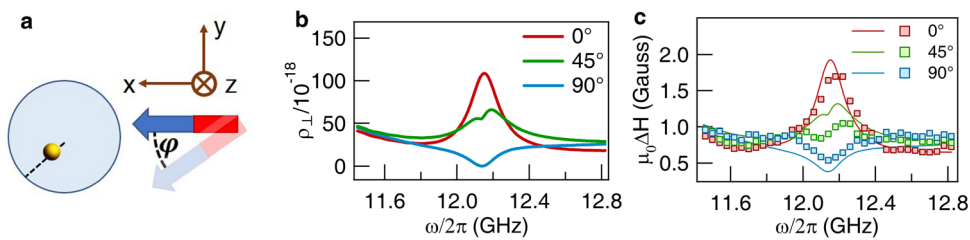


**Fig. 3 LDOS (local density of photon states) polarization dependence.** **a** Schematic of tuning orientation of external magnetic field  $H$  relative to the  $\hat{x}$ -direction in the plane of waveguide cross-section. **b** Simulated photon LDOS perpendicular to external magnetic field  $H$  with relative angles of  $\varphi = 0^\circ$ ,  $45^\circ$ , and  $90^\circ$ . **c** Measured magnon linewidth spectra, that is,  $\mu_0\Delta H - \omega$  relation (squares) and calculated results (solid lines) for different angles of  $\varphi = 0^\circ$ ,  $45^\circ$ , and  $90^\circ$ . Errors of linewidth fit are smaller than the size of symbols.

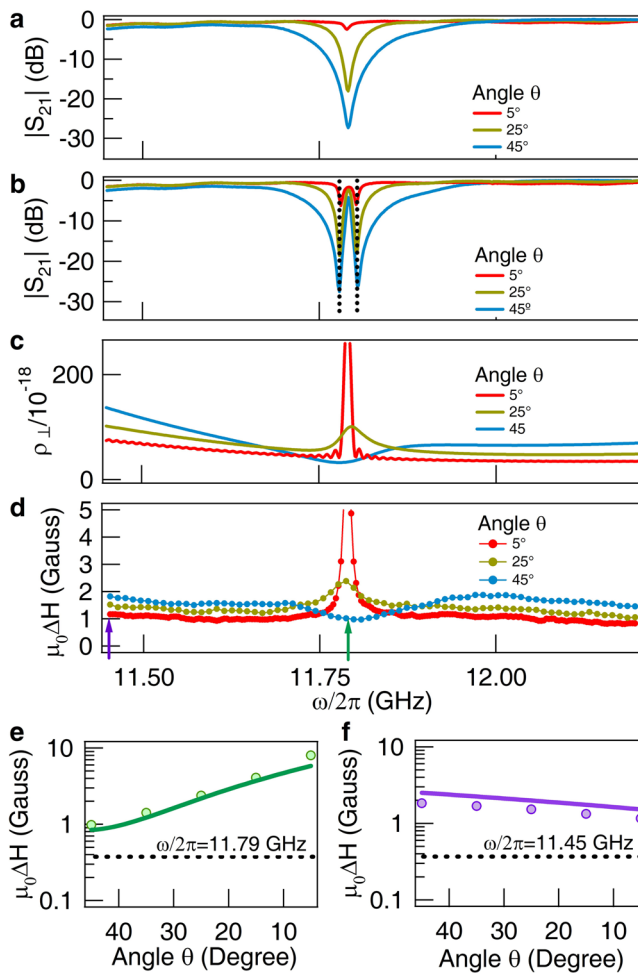


**Fig. 4 Cavity geometry dependence.** **a** Cavity mode transmission profile when rotating the relative angle  $\theta$ . **b** Rabi splitting spectra for different angles  $\theta$ . **c** Simulated LDOS (local density of photon states)  $\rho_\perp$  for different  $\theta$ . **d** Measured magnon linewidth spectra ( $\mu_0\Delta H - \omega$  relation) when tuning the relative angle  $\theta$ . **e**, **f** shows comparison between theoretical results and measurement at 11.79 GHz cavity resonance (**e**) and 11.45 GHz continuous-wave frequency (**f**). The dashed lines are intrinsic linewidths of the YIG (Yttrium iron garnet) sphere. Errors of linewidth fit are smaller than the size of symbols.

transitions can be smoothly adjusted. By tuning the angle  $\theta$  from  $45^\circ$  to  $5^\circ$ , our system shows a significant change in photon transmission as illustrated in Fig. 4a, accompanied by significant enhancements in the cavity quality factor and global density of states<sup>44,45</sup>. In addition the cavity resonance shows a redshift to 11.79 GHz due to the increase in cavity length. The YIG sphere is placed at the center of the cavity cross-section with  $d = 6$  mm,

and the external magnetic field is applied in the  $\hat{x}$ -direction. These experimental conditions provide stable magnon–photon coupling strength when  $\theta$  is tuned, as shown by the nearly unchanged mode splitting in Fig. 4b.

Our hybrid system now readily allows us to investigate the magnon radiation controlled by cavity geometry. In particular, tuning the relative angle  $\theta$  from  $45^\circ$  to  $5^\circ$  leads to a redistribution of photon states in the cavity, greatly enhancing the LDOS near the cavity resonance and allowing the continuous-wave LDOS to be controlled in the opposite way, as illustrated by the simulated LDOS  $\rho_\perp$  in Fig. 4c. Based on the theoretical model, we expect that the magnon linewidth can quantitatively follow the geometry-controlled LDOS  $\rho_\perp$ . The results from measurements under different  $\theta$  are shown in Fig. 4d, and we indeed obtain linewidth  $\mu_0\Delta H$  with similar behavior to that of the simulated LDOS  $\rho_\perp$ . As is evident in Fig. 4e, f, we find that the linewidth is well reproduced by our theoretical model with  $\kappa R$  adjusted to  $4.3 \times 10^{22} \text{ m}^3 \text{s}^{-2}$ . By tuning LDOS via the relative angle  $\theta$ , the experimental linewidth is enhanced 20-fold at the cavity resonance in comparison with the intrinsic damping of the magnon, as illustrated by the dashed lines.

## Discussion

Understanding and controlling magnon radiative damping is essential in tuning the magnon lifetime and transporting spin information by travelling photons in magnonic or spintronic applications<sup>27–29,46,47</sup>. By revealing the quantitative relation between magnon radiative damping and photon LDOS for the first time, to the best of our knowledge, our work introduces three perspectives for better exploring and using magnon radiation in future research.

**Flexible control of magnon lifetime.** Photon LDOS construction can flexibly tune the magnon lifetime on the basis of intrinsic Gilbert damping. Magnon with a long lifetime is useful for information storage and memory, while magnon with a suppressed lifetime would bring an advantageous impact for realizing a fast repetition rate in the device<sup>29</sup>. Our work explores some techniques including LDOS magnitude, polarization and global environment to control magnon radiative damping, which could open paths for various methods for controlling the LDOS to tune the magnon lifetime in a flexible and precise fashion and provides a new ingredient to advanced communication processing<sup>48</sup>.

**Delivering coherent information of cavity-magnon polariton to open systems.** Although the weak interaction between the magnetic dipole and photons can be enhanced by confining the photon mode in a cavity, the confinement restricts the information of the closed system to be efficiently transferred to the open system and vice versa. Our constructed magnon–photon system can combine both the standing and travelling photon modes to

couple the magnon mode. The traveling channel allows us to deliver the coherent information out, thus advancing the efficient tuning of the dynamics of the cavity-magnon polariton. Manipulation of magnon radiation to an open system, as we demonstrated, is very attractive for exploring new physics related to magnon dissipative precession<sup>49</sup>, such as dissipative coupling in a magnon-based hybrid system<sup>50</sup>.

**Stimulating the advancement of hybrid magnonics.** Controllable magnon radiation could stimulate hybrid magnonic systems to access new frontiers. Recent studies show that coherent information at a single magnon level can be coherently transferred to a photon or superconducting qubit through radiation at millikelvin temperatures<sup>14,51</sup>, revealing the quantum nature to the hybridized magnonic system. At room temperature, the magnon–photon mode coupling is generally restricted in linear harmonic dynamics, while recent research breaks this harmonic restriction by using a feedback mechanism, exhibiting nonlinear triplet spectra similar to quantum dots<sup>21</sup>. Controlling magnon radiation in these new regimes could stimulate the advancement of hybrid magnonics.

In conclusion, we observe and show the ability to control the photon emission from magnon and magnon radiative damping in the hybrid magnon–photon system, bridging their relation to the tunable photon LDOS. One quantitative method to design and tune the radiation efficiency of the magnon is provided based on tailoring the photon LDOS including LDOS magnitude and/or polarization, thereby possibly leading to a general technique of tuning magnon relaxation on demand. Our measurements are mainly performed in the MIT regime with large photon damping, which causes radiative damping by photon dissipation, while travelling-wave photons can directly transfer the magnon energy to an open system. Overall, our study introduces a mechanism to coherently manipulate magnon dynamics by local photon states and suggests a promising potential toward the development of magnon-based hybrid devices and related coherent information processing.

## Methods

**Device description.** Our waveguide cavity is made up of a cylindrical waveguide and two circular rectangular transitions coaxially connected at both ends. Through the transition, a smooth change between  $TE_{10}$  mode of rectangular waveguide port and  $TE_{11}$  one of cylindrical waveguide can be established. Via coaxial cables, the cavity is connected to the input/output ports of a VNA. With an input power of 0 dBm, the transmission signals can be precisely picked up by VNA. YIG sphere is fixed firmly inside the cavity with scotch tape, with its location tunable on demand to couple with different microwave magnetic fields. YIG and the scotch tape, as dielectric materials, can slightly influence the microwave fields distribution in our experiment. We neglect the small dielectric influence in our theoretical treatment.

**Theoretical description.** In Supplementary Note 1, the theory of magnon spontaneous radiation in the waveguide including the derivation of the magnon linewidth induced by the LDOS is provided.

## Data availability

The data that support the findings of this study are available from the corresponding authors upon reasonable request.

Received: 12 September 2019; Accepted: 25 November 2019;

Published online: 13 December 2019

## References

- Lenk, B., Ulrichs, H., Garbs, F. & Münzenberg, M. The building blocks of magnonics. *Phys. Rep.* **507**, 107–136 (2011).
- Chumak, A. V., Vasylchuk, V. I., Serga, A. A. & Hillebrands, B. Magnon spintronics. *Nat. Phys.* **11**, 453 (2015).
- Grundler, D. Spintronics: nanomagnonics around the corner. *Phys. Rep.* **11**, 407 (2016).
- Demidov, V. E. et al. Magnetization oscillations and waves driven by pure spin currents. *Phys. Rep.* **673**, 1–31 (2017).
- Tserkovnyak, Y., Brataas, A. & Bauer, G. E. Enhanced Gilbert damping in thin ferromagnetic films. *Phys. Rev. Lett.* **88**, 117601 (2002).
- Tserkovnyak, Y., Brataas, A., Bauer, G. E. & Halperin, B. I. Nonlocal magnetization dynamics in ferromagnetic heterostructures. *Rev. Mod. Phys.* **77**, 1375 (2005).
- Kamra, A., Keshtgar, H., Yan, P. & Bauer, G. E. Coherent elastic excitation of spin waves. *Phys. Rev. B* **91**, 104409 (2015).
- Streib, S., Keshtgar, H. & Bauer, G. E. Damping of magnetization dynamics by phonon pumping. *Phys. Rev. Lett.* **121**, 027202 (2018).
- Yu, T., Liu, C., Yu, H., Blanter, Y. M. & Bauer, G. E. Chiral excitation of spin waves in ferromagnetic films by magnetic nanowire gratings. *Phys. Rev. B* **99**, 134424 (2019).
- Chen, J. et al. Excitation of unidirectional exchange spin waves by a nanoscale magnetic grating. *Phys. Rev. B* **100**, 104427 (2019).
- Jackson, J. D. *Classical Electrodynamics* (Wiley, New York, 1998).
- Chang, H. et al. Nanometer-thick yttrium iron garnet films with extremely low damping. *IEEE Magn. Lett.* **5**, 6700104 (2014).
- Cao, Y. et al. Exchange magnon-polaritons in microwave cavities. *Phys. Rev. B* **91**, 094423 (2015).
- Tabuchi, Y. et al. Coherent coupling between a ferromagnetic magnon and a superconducting qubit. *Science* **349**, 405 (2015).
- Soykal, Ö. O. & Flatté, M. E. Strong field interactions between a nanomagnet and a photonic cavity. *Phys. Rev. Lett.* **104**, 077202 (2010).
- Huebl, H. et al. High cooperativity in coupled microwave resonator ferrimagnetic insulator hybrids. *Phys. Rev. Lett.* **111**, 127003 (2013).
- Goryachev, M. et al. High-cooperativity cavity QED with magnons at microwave frequencies. *Phys. Rev. Appl.* **2**, 054002 (2014).
- Zhang, X., Zou, C. L., Jiang, L. & Tang, H. X. Strongly coupled magnons and cavity microwave photons. *Phys. Rev. Lett.* **113**, 156401 (2014).
- Bai, L. et al. Spin pumping in electro-dynamically coupled magnon-photon systems. *Phys. Rev. Lett.* **114**, 227201 (2015).
- Wang, Y. P. Bistability of cavity magnon polaritons. *Phys. Rev. Lett.* **120**, 057202 (2018).
- Yao, B. M. et al. Cooperative polariton dynamics in feedback-coupled cavities. *Nat. Commun.* **8**, 1437 (2017).
- Söllner, I. N. et al. Deterministic photon-emitter coupling in chiral photonic circuits. *Nat. Nanotechnol.* **10**, 775–778 (2015).
- Young, A. B. et al. Polarization engineering in photonic crystal waveguides for spin-photon entanglers. *Phys. Rev. Lett.* **115**, 153901 (2015).
- Bloembergen, N. & Pound, R. V. Radiation damping in magnetic resonance experiments. *Phys. Rev.* **95**, 8 (1954).
- Sanders, R. W., Paquette, D., Jaccarino, V. & Rezende, S. M. Radiation damping in magnetic resonance. II. Continuous-wave antiferromagnetic-resonance experiments. *Phys. Rev. B* **10**, 132 (1974).
- Schoen, M. A. W., Shaw, J. M., Nembach, H. T., Weiler, M. & Silva, T. J. Radiative damping in waveguide-based ferromagnetic resonance measured via analysis of perpendicularly standing spin waves in sputtered permalloy films. *Phys. Rev. B* **92**, 184417 (2015).
- Frimmer, M. & Koenderink, A. F. Spontaneous emission control in a tunable hybrid photonic system. *Phys. Rev. Lett.* **110**, 217405 (2013).
- Lodahl, P. et al. Controlling the dynamics of spontaneous emission from quantum dots by photonic crystals. *Nature* **430**, 654 (2004).
- Bienfait, A. et al. Controlling spin relaxation with a cavity. *Nature* **531**, 74 (2016).
- Feber, B. I., Rotenberg, N. & Kuipers, L. Nanophotonic control of circular dipole emission. *Nat. Commun.* **6**, 6695 (2015).
- Lu, D., Kan, J. J., Fullerton, E. E. & Liu, Z. W. Enhancing spontaneous emission rates of molecules using nanopatterned multilayer hyperbolic metamaterials. *Nat. Nanotechnol.* **9**, 48–53 (2014).
- Xiang, Z. L., Ashhab, S., You, J. Q. & Nori, F. Hybrid quantum circuits: superconducting circuits interacting with other quantum systems. *Rev. Mod. Phys.* **85**, 623 (2013).
- Yao, B. M. et al. Theory and experiment on cavity magnon-polariton in the one-dimensional configuration. *Phys. Rev. B* **92**, 184407 (2015).
- Yao, B. M. et al. Quantifying the complex permittivity and permeability of magnetic nanoparticles. *Appl. Phys. Lett.* **106**, 142406 (2015).
- Langguth, L., Fleury, R., Alù, A. & Koenderink, A. F. Drexhage's experiment for sound. *Phys. Rev. Lett.* **116**, 224301 (2016).
- Noda, S., Fujita, M. & Asano, T. Spontaneous-emission control by photonic crystals and nanocavities. *Nat. Photonics* **1**, 449 (2007).
- Miroshnichenko, A. E., Flach, S. & Kivshar, Y. S. Fano resonances in nanoscale structures. *Rev. Mod. Phys.* **82**, 2257 (2010).
- Maleki, L., Matsko, A. B., Savchenkov, A. A. & Ilchenko, V. S. Tunable delay line with interacting whispering-gallery-mode resonators. *Opt. Lett.* **29**, 626–628 (2004).

39. Miroshnichenko, A. E., Mingaleev, S. F., Flach, S. & Kivshar, Y. S. Nonlinear Fano resonance and bistable wave transmission. *Phys. Rev. E* **71**, 036626 (2005).
40. Fano, U. Effects of configuration interaction on intensities and phase shifts. *Phys. Rev.* **124**, 1866 (1961).
41. Jevons, W. & Shenstone, A. G. Spectroscopy: I. atomic spectra. *Rep. Progr. Phys.* **5**, 210–227 (1938).
42. Gui, Y. S., Wirthmann, A., Mecking, N. & Hu, C.-M. Direct measurement of nonlinear ferromagnetic damping via the intrinsic foldover effect. *Phys. Rev. B* **80**, 060402(R) (2009).
43. Bai, L. H. et al. Control of the magnon–photon coupling. *IEEE Trans. Magn.* **52**, 1000107 (2016).
44. Wigner, E. Lower limit for the energy derivative of the scattering phase shift. *Phys. Rev.* **98**, 145 (1955).
45. Smith, F. T. Lifetime matrix in collision theory. *Phys. Rev.* **118**, 349 (1960).
46. Kimble, H. J. The quantum internet. *Nature* **453**, 1023 (2008).
47. Wallquist, M., Hammerer, K., Rabl, P., Lukin, M. & Zoller, P. Hybrid quantum devices and quantum engineering. *Phys. Scr.* **T137**, 014001 (2009).
48. Zhang, X. et al. Magnon dark modes and gradient memory. *Nat. Commun.* **6**, 8914 (2015).
49. Harder, M. et al. Level attraction due to dissipative magnon–photon coupling. *Phys. Rev. Lett.* **121**, 137203 (2018).
50. Lachance-Quirion, D., Tabuchi, Y., Gloppe, A., Usami, K. & Nakamura, Y. Hybrid quantum systems based on magnonics. *Appl. Phys. Express* **12**, 070101 (2019).
51. Tabuchi, Y. et al. Hybridizing ferromagnetic magnons and microwave photons in the quantum limit. *Phys. Rev. Lett.* **113**, 083603 (2014).

## Acknowledgements

T.Y. was supported by the Netherland Organization for Scientific Research (NWO). This work was funded by the National Natural Science Foundation of China under Grant Nos. 11974369 and 11804352, the Shanghai Pujiang Program No. 18PJ1410600, SITP Innovation Foundation (CX-245), and Independent Research Project of State Key Laboratory of Infrared Physics (No. Z201920). We would like to thank Y. Zhao, J. Sirker, L.H. Bai, P. Hyde, Y.M. Blanter, and G.E.W. Bauer for useful discussions.

## Author contributions

B.Y. and Y.S.G. set up the hybrid system and conducted the experiment, as well as analyzed the data. T.Y., in discussions with B.Y. and C.-M.H., developed the theory

part. J.W.R. and Y.T.Z. contributed to the design of the cavity parts. B.Y. and T.Y. prepared all the figures as well as the Supplementary Information. T.Y., W.L. and C.-M.H. together supervised the work. All authors contributed to writing the paper.

## Competing interests

The authors declare no competing interests.

## Additional information

**Supplementary information** is available for this paper at <https://doi.org/10.1038/s42005-019-0264-z>.

**Correspondence** and requests for materials should be addressed to T.Y., W.L. or C.-M.H.

**Reprints and permission information** is available at <http://www.nature.com/reprints>

**Publisher's note** Springer Nature remains neutral with regard to jurisdictional claims in published maps and institutional affiliations.



**Open Access** This article is licensed under a Creative Commons Attribution 4.0 International License, which permits use, sharing, adaptation, distribution and reproduction in any medium or format, as long as you give appropriate credit to the original author(s) and the source, provide a link to the Creative Commons license, and indicate if changes were made. The images or other third party material in this article are included in the article's Creative Commons license, unless indicated otherwise in a credit line to the material. If material is not included in the article's Creative Commons license and your intended use is not permitted by statutory regulation or exceeds the permitted use, you will need to obtain permission directly from the copyright holder. To view a copy of this license, visit <http://creativecommons.org/licenses/by/4.0/>.

© The Author(s) 2019

## Supplementary Information

### 1 Supplementary Note 1.

#### Theory of magnon spontaneous radiation

In this part, we describe the model about the magnon spontaneous radiation in a waveguide. We first set up the Fano-Anderson Hamiltonian for the magnon-photon coupling in a waveguide [1, 2], and then calculate the energy broadening due to the magnon spontaneous radiation.

##### 1.1 Hamiltonian

The free energy of the coupled system is written as [3]

$$F = F_0(\mathbf{M}) + \frac{\epsilon_0}{2} \int d\mathbf{r} \mathbf{E}(\mathbf{r}) \cdot \mathbf{E}(\mathbf{r}) + \frac{\mu_0}{2} \int d\mathbf{r} \mathbf{H}(\mathbf{r}) \cdot \mathbf{H}(\mathbf{r}) + \mu_0 \int d\mathbf{r} \mathbf{H}(\mathbf{r}) \cdot \mathbf{M}(\mathbf{r}), \quad (1)$$

where  $\epsilon_0$  and  $\mu_0$  are the vacuum dielectric and permeability constants, respectively.  $F_0(\mathbf{M})$  describes the free energy of magnetization  $\mathbf{M}$ , the second and third terms denote the free energy of electromagnetic waves due to the electric field  $\mathbf{E}$  and magnetic field  $\mathbf{H}$  in a waveguide, and the last term represents the Zeeman interaction between the magnetization and the magnetic field. The Hamiltonian can be obtained by quantizing the free energy.

Due to the long-wavelength nature of the electromagnetic waves in the waveguide we are considering, only the uniform precession of the magnetization, i.e., the Kittel mode [4], needs to be considered. We express  $\mathbf{M} = -\gamma\hbar\mathbf{S}$  in terms of the spin operators [4, 5, 6], where  $\gamma$  is modulus of the gyromagnetic ratio. The spin operators are expanded by magnon operator  $\hat{\alpha}_K$  in the Kittel mode [4, 5, 6],

$$\hat{S}_\beta^K = \sqrt{2S} [M_\beta^K \hat{\alpha}_K(t) + (M_\beta^K)^* \hat{\alpha}_K^\dagger(t)], \quad (2)$$

in which  $\beta = \{z, x\}$  assuming that the equilibrium magnetization is along the  $\hat{\mathbf{y}}$ -direction.  $S = M_s/(\gamma\hbar)$  with  $M_s$  being the saturated magnetization;  $M_\beta^K$  is the amplitude of the Kittel mode that is normalized according to [7, 8]

$$\int d\mathbf{r} [M_z^K(\mathbf{r})(M_x^K(\mathbf{r}))^* - (M_z^K(\mathbf{r}))^* M_x^K(\mathbf{r})] = -i/2. \quad (3)$$

Because the magnetization is uniform in the magnetic sphere and the Kittel mode is circularly polarized with  $M_x = iM_z$ , we obtain

$$M_z^K = 1/(2\sqrt{V_s}), \quad (4)$$

in which  $V_s$  is the volume of the magnetic sphere.

In the waveguide, the electromagnetic field operators are expanded by the photon operator  $a_{k,\lambda}$  in which  $k > 0$  is the momentum of photon along the waveguide, i.e., the  $\hat{\mathbf{z}}$ -direction, and  $\lambda$  ( $\mu$  below) labels

the eigenmodes in the waveguide [3],

$$\begin{aligned}\mathbf{E}(\mathbf{r}) &= \sum_{\lambda,k} [\mathbf{E}_k^\lambda(x,y)e^{ikz}\hat{a}_{k,\lambda} + \mathbf{E}_{-k}^\lambda(x,y)e^{-ikz}\hat{a}_{-k,\lambda} + \text{h.c.}], \\ \mathbf{H}(\mathbf{r}) &= \sum_{\lambda,k} [\mathbf{H}_k^\lambda(x,y)e^{ikz}\hat{a}_{k,\lambda} + \mathbf{H}_{-k}^\lambda(x,y)e^{-ikz}\hat{a}_{-k,\lambda} + \text{h.c.}],\end{aligned}\quad (5)$$

where the eigenmodes of electric and magnetic fields are expressed as [3]

$$\mathbf{E}_k^\lambda(x,y,z) = \frac{1}{\sqrt{L}} [\mathcal{E}_k^{t\lambda}(x,y) + \mathcal{E}_{kz}^\lambda(x,y)\hat{\mathbf{z}}] e^{ikz}, \quad \mathbf{H}_k^\lambda(x,y,z) = \frac{1}{\sqrt{L}} [\mathcal{H}_k^{t\lambda}(x,y) + \mathcal{H}_{kz}^\lambda(x,y)\hat{\mathbf{z}}] e^{ikz}, \quad (6)$$

$$\mathbf{E}_{-k}^\lambda(x,y,z) = \frac{1}{\sqrt{L}} [\mathcal{E}_k^{t\lambda}(x,y) - \mathcal{E}_{kz}^\lambda(x,y)\hat{\mathbf{z}}] e^{-ikz}, \quad \mathbf{H}_{-k}^\lambda(x,y,z) = \frac{1}{\sqrt{L}} [-\mathcal{H}_k^{t\lambda}(x,y) + \mathcal{H}_{kz}^\lambda(x,y)\hat{\mathbf{z}}] e^{-ikz} \quad (7)$$

Here, “*t*” means “transverse”, and *L* is the length of the waveguide. The eigenmodes satisfy the following orthonormal relations [3],

$$\begin{aligned}\int \mathcal{E}_k^{t\lambda} \cdot \mathcal{E}_{k'}^{t\mu} da &= \delta_{kk'}\delta_{\lambda\mu} A_k^\lambda, \\ \int \mathcal{H}_k^{t\lambda} \cdot \mathcal{H}_{k'}^{t\mu} da &= \frac{1}{(Z_k^\lambda)^2} \delta_{kk'}\delta_{\lambda\mu} A_k^\lambda, \\ \int \mathcal{E}_{k,z}^\lambda \mathcal{E}_{k',z}^\mu da &= -\frac{\gamma_\lambda^2}{k^2} \delta_{kk'}\delta_{\lambda\mu} A_k^\lambda, \quad (\text{TM}) \\ \int \mathcal{H}_{k,z}^\lambda \mathcal{H}_{k',z}^\mu da &= -\frac{\gamma_\lambda^2}{k^2(Z_k^\lambda)^2} \delta_{kk'}\delta_{\lambda\mu} A_k^\lambda, \quad (\text{TE}) \\ \frac{1}{2} \int (\mathcal{E}_k^{t\lambda} \times \mathcal{H}_{k'}^{t\mu}) \cdot \hat{\mathbf{z}} da &= \frac{1}{2Z_k^\lambda} \delta_{kk'}\delta_{\lambda\mu} A_k^\lambda,\end{aligned}\quad (8)$$

where  $Z_k^\lambda = \mu_0\omega_k^\lambda/k$  and  $k/(\epsilon_0\omega_k^\lambda)$  are the impedances for the TE and TM modes,  $A_k^\lambda = \hbar\omega_k^\lambda/(2\epsilon_0)$  and  $\hbar/(2\epsilon_0\omega_k^\lambda)$  for the TE and TM modes with  $\omega_k^\lambda$  being the eigen-energy, and

$$\gamma_\lambda^2 = \mu_0\epsilon_0(\omega_k^\lambda)^2 - k^2 = (\omega_k^\lambda)^2/c^2 - k^2. \quad (9)$$

Please note that  $\omega_k^\lambda = c\sqrt{k^2 + \gamma_\lambda^2}$  in which  $\gamma_\lambda$  only depends on the band but not the momentum is understood. With these orthonormal relations, we demonstrate

$$\frac{\epsilon_0}{2} \int d\mathbf{r} \mathbf{E}(\mathbf{r}) \cdot \mathbf{E}(\mathbf{r}) + \frac{\mu_0}{2} \int d\mathbf{r} \mathbf{H}(\mathbf{r}) \cdot \mathbf{H}(\mathbf{r}) = \sum_{k,\lambda} \hbar\omega_k^\lambda (\hat{a}_{k,\lambda}^\dagger \hat{a}_{k,\lambda} + \hat{a}_{-k,\lambda}^\dagger \hat{a}_{-k,\lambda}). \quad (10)$$

With the established magnon and photon operators, the coupling Hamiltonian is constructed,

$$\hat{H}_{\text{int}} = \mu_0 \int d\mathbf{r} \mathbf{H}(\mathbf{r}) \cdot \mathbf{M}(\mathbf{r}) = -\mu_0\gamma\hbar \int d\mathbf{r} (\hat{H}_x \hat{S}_x + \hat{H}_z \hat{S}_z). \quad (11)$$

By assuming the magnetic sphere is small located at  $(x_0, y_0, z_0)$ , this Hamiltonian is calculated to be

$$\hat{H}_{\text{int}} = \hbar \sum_{k_z=\pm k,\lambda} (g_{k_z,\lambda} \hat{a}_{k_z,\lambda} \hat{a}_K^\dagger + h_{k_z,\lambda} \hat{a}_{k_z,\lambda} \hat{a}_K + \text{h.c.}), \quad (12)$$

where the coupling strength reads

$$g_{k_z,\lambda} = \frac{\mu_0}{2} \sqrt{\frac{2\gamma M_s V_s}{\hbar L A_k^\lambda}} [i\mathcal{H}_{k_z,x}^\lambda(x_0, y_0) - \mathcal{H}_{k_z,z}^\lambda(x_0, y_0)] e^{ik_z z_0}. \quad (13)$$

as we can see here, as the static field *H* is assumed at y direction, the coupling effect between magnon and cavity photon states is determined by a combination of eigenmodes that perpendicular to *H*.

## 1.2 Spontaneous radiation

From above calculation, the whole Hamiltonian for a magnetic sphere in the waveguide is written as

$$H_0/\hbar = \omega_K \hat{a}_K^\dagger \hat{a}_K + \sum_{k_z} \omega_{k_z} \hat{a}_{k_z}^\dagger \hat{a}_{k_z} + \sum_{k_z} g_{k_z} (\hat{a}_K^\dagger \hat{a}_{k_z} + \hat{a}_K \hat{a}_{k_z}^\dagger), \quad (14)$$

in which  $k_z = \pm k$  and the band index for photon is disregarded when only the lowest band is considered here. This Hamiltonian is known as the Fano-Anderson Hamiltonian with an exact solution being possible [1, 2]. The lifetime of magnon can be calculated from the imaginary part of the self-energy [2] that is interpreted to come from the spontaneous radiation of magnon [1]. The Green function of Kittel magnon is exactly calculated to be

$$G_m(\omega) = \left\{ \hbar\omega - \hbar\omega_K + i\delta_K - \sum_{k_z} \frac{|\hbar g_{k_z}|^2}{\hbar\omega - \hbar\omega_{k_z} + i\delta_{k_z}} \right\}^{-1}, \quad (15)$$

where  $\delta_K = \alpha\omega_K$  is the intrinsic Gilbert damping of Kittel magnon with  $\alpha$  being the intrinsic Gilbert damping coefficient. The imaginary part of the self-energy, i.e.,  $\sum_{k_z} \frac{|\hbar g_{k_z}|^2}{\hbar\omega - \hbar\omega_{k_z} + i\delta_{k_z}}$ , contributes to the broadening of the magnon spectra. Therefore the total broadening of magnon reads

$$\Delta E_K = \delta_K + \pi \sum_{k_z} |\hbar g_{k_z}|^2 \delta(\hbar\omega_K - \hbar\omega_{k_z}) = \delta_K + \frac{\pi}{\hbar} |\hbar g(\omega_K)|^2 \mathcal{D}(\omega_K), \quad (16)$$

where  $\mathcal{D}(\omega_K)$  is the global density of states (DOS) of photon in the waveguide.

By further defining the width in terms of the magnetic field  $\Delta E = \hbar\gamma\mu_0\Delta H$ , we obtain

$$\mu_0\Delta H = \frac{\alpha\omega_K}{\gamma} + \frac{\pi}{\gamma} |g(\omega_K)|^2 \mathcal{D}(\omega_K) = \frac{\alpha\omega_K}{\gamma} + \frac{2\pi}{\gamma} \xi |g_{\text{CST}}(\omega_K)|^2. \quad (17)$$

For TE mode in the experiment, parameter  $\xi$  is expressed as

$$\xi = \frac{1}{2} \left( \frac{\mu_0}{2} \sqrt{\frac{2\gamma M_s V_s}{\hbar}} \sqrt{\frac{\hbar\omega_K}{2\epsilon_0 c\sqrt{\pi\mu_0}}} \right)^2. \quad (18)$$

In Supplementary Eq. (17), another coupling strength  $g_{\text{CST}}$  is defined when the normalization with unit power flow in waveguide is used in the *Computer simulation technology* (CST) [3], i.e.,

$$\frac{1}{2} \int (\tilde{\mathcal{E}}_k^{t\lambda} \times \tilde{\mathcal{H}}_{k'}^{t\mu}) \cdot \hat{\mathbf{z}} da = \frac{1}{2} \delta_{kk'} \delta_{\lambda\mu}. \quad (19)$$

The relation between  $\{\tilde{\mathcal{E}}_k, \tilde{\mathcal{H}}_k\}$  here and  $\{\mathcal{E}_k, \mathcal{H}_k\}$  in Eqs. (8) reads

$$\{\tilde{\mathcal{E}}_k, \tilde{\mathcal{H}}_k\} = \{\mathcal{E}_k, \mathcal{H}_k\} \times c\sqrt{\pi\mu_0} \sqrt{\mathcal{D}/(A_k L)}. \quad (20)$$

It is seen that  $g_{\text{CST}}$  is proportional to the local field strength and  $\sqrt{\mathcal{D}}$ .

## 1.3 Relation to local density of states

Although the CST does not directly calculate the local density of photon states (LDOS), we can show  $|g_{\text{CST}}|^2$  is indeed proportional to the LDOS. To define the magnetic-field LDOS *in the TE mode* [9], we

define the new eigenmodes with different orthonormal conditions from Eqs. (8),

$$\begin{aligned}\int (\bar{\mathcal{H}}_k^{t\lambda})^* \cdot \bar{\mathcal{H}}_{k'}^{t\mu} da &= \int \bar{\mathcal{H}}_k^{t\lambda} \cdot \bar{\mathcal{H}}_{k'}^{t\mu} da = \delta_{kk'} \delta_{\lambda\mu} (B_k^\lambda)^2 / \mu_0, \\ \int (\bar{\mathcal{H}}_{k,z}^\lambda)^* \bar{\mathcal{H}}_{k',z}^\mu da &= - \int \bar{\mathcal{H}}_{k,z}^\lambda \bar{\mathcal{H}}_{k',z}^\mu da = \frac{\gamma_\lambda^2}{k^2} \delta_{kk'} \delta_{\lambda\mu} (B_k^\lambda)^2 / \mu_0,\end{aligned}\quad (21)$$

where  $B_k^\lambda = ck/\omega_k^\lambda$ . This means

$$\bar{\mathcal{H}}_k^\lambda = \mathcal{H}_k^\lambda \times \frac{Z_k^\lambda B_k^\lambda}{\sqrt{\mu_0} \sqrt{A_k^\lambda}}. \quad (22)$$

With these conditions, for the waveguide with uniform section, i.e., with translation symmetry, the magnetic-field LDOS per unit length is defined by [9]

$$\rho_\alpha(x, y, \omega) = \frac{1}{L} \mu_0 \sum_{k,\lambda} \delta(\omega - \omega_k^\lambda) |\bar{\mathcal{H}}_{k,\alpha}(x, y)|^2, \quad (23)$$

with  $\alpha = \{x, y, z\}$ . From the normalization condition in Eqs. (21), it is checked that  $\sum_\alpha \int dx dy \rho_\alpha(x, y, \omega) = \mathcal{D}(\omega)/L$ . When  $\lambda$  is the lowest TE mode, we find that

$$\rho_\alpha(x, y, \omega) = \frac{1}{L} \mu_0 \mathcal{D}(\omega) |\bar{\mathcal{H}}_{k,\alpha}(x, y)|^2. \quad (24)$$

This leads to

$$\begin{aligned}|g(\omega)|^2 \mathcal{D}(\omega) &= \xi |g_{\text{CST}}(\omega)|^2 = \left(\frac{\mu_0}{2}\right)^2 \frac{2\gamma M_s V_s}{\hbar L A_k^\lambda} [|H_z^k(x_0, y_0)|^2 + |H_x^k(x_0, y_0)|^2] \mathcal{D}(\omega) \\ &= \frac{\gamma M_s V_s}{2\hbar c^2} \rho_\perp(x_0, y_0, \omega) \equiv \kappa \rho_\perp(x_0, y_0, \omega),\end{aligned}\quad (25)$$

where  $\kappa = \frac{\gamma M_s V_s}{2\hbar c^2}$  and  $\rho_\perp(x_0, y_0, \omega) = \rho_z(x_0, y_0, \omega) + \rho_x(x_0, y_0, \omega)$ . Thus, for waveguide with uniform section,

$$\rho_\perp(x_0, y_0, \omega) = \xi |g_{\text{CST}}|^2 / \kappa, \quad (26)$$

that can be determined by CST simulation approach. Finally, we can reach

$$\mu_0 \Delta H = \mu_0 \Delta H_0 + \frac{\alpha \omega_K}{\gamma} + \frac{2\pi\kappa}{\gamma} R |\rho_\perp(x_0, y_0, \omega)| |\mathcal{LDOS}|, \quad (27)$$

in which  $|\mathcal{LDOS}| \equiv 1 \text{ m}^{-3} \cdot \text{s}$  explicitly represents the unit of LDOS for photons,  $\mu_0 \Delta H_0$  is the inhomogeneous broadening of magnon linewidth at zero frequency and  $R$  is a fitting parameter mainly influenced by cavity design and cable loss in practical measurement circuit.

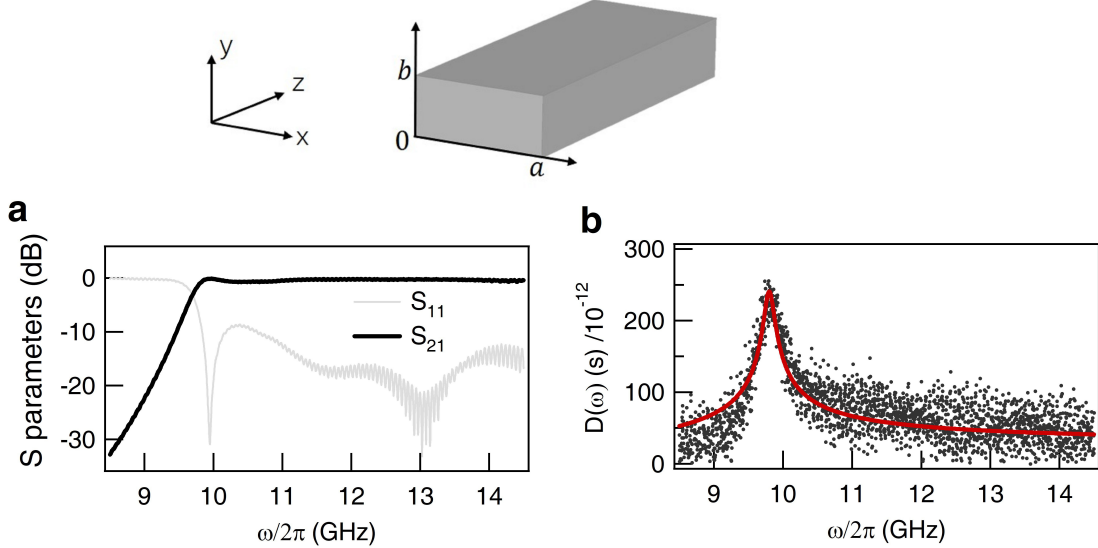
Above theory is established for the ideal waveguide with the same cross section along the waveguide. When the cross section slowly varies as the case in our experiment, this treatment can be still a good approximation, with the fitting parameter quantity  $R \sim 0.8$  that is close to unity. A direct comparison between the theory and experiment in ideal waveguide is presented in the following section.

## 2 Supplementary Note 2.

### Magnon linewidth enhancement in rectangular waveguide

#### 2.1 Enhanced DOS near waveguide cut-off frequency

In this part, the enhancement of DOS of photon near the cut-off frequency of a standard rectangular waveguide is measured. A rectangular waveguide that works at Ku band ( $a = 15.8$  mm and  $b = 7.8$  mm) is used for constructing photon states, as schematically shown in Supplementary Fig. 1. The transmission  $|S_{21}|$  as well as the reflection  $|S_{11}|$  signals are measured by an Vector Network analyzer (VNA) with an input power of 0 dbm, as shown in Supplementary Fig. 1(a).  $S_{21}$  amplitude is observed to decrease below the cut-off frequency  $\omega_{\text{cut}}/2\pi=9.8$  GHz of our device because the microwave becomes evanescent with larger wavelength.



Supplementary Figure 1: **Photonic structure of rectangular waveguide.** (a)  $S$ -matrix parameters for Ku-band rectangular waveguide. (b) Calculated microwave photon DOS (global density of states) for the rectangular waveguide (dots) with fit line (solid lines).

Physically, near the cut-off frequency, the magnitude of the momentum for the microwaves tends to be zero along the propagation direction, leading to an enhancement of global DOS  $D(\omega)$  near cut-off frequency. This effect can be verified by obtaining the global DOS from  $S$ -matrix parameters via the inversion relation [10, 11],

$$\mathcal{D}(\omega) = -i(1/2\pi V) \text{Tr}(S^\dagger dS/d\omega), \quad (28)$$

where  $S(\omega) = \begin{pmatrix} S_{11}(\omega) & S_{12}(\omega) \\ S_{21}(\omega) & S_{22}(\omega) \end{pmatrix}$  represents the scattering matrix. From the measured  $S$  parameters, we can plot DOS in Supplementary Fig. 1(b), in which an enhancement of DOS near the cut-off frequency

is clearly observed.

Analytically, the global DOS for photons in the TE<sub>10</sub> mode in a rectangular waveguide is calculated to be [3]

$$\mathcal{D}(\omega) = \sum_{k_z} \delta(\omega - \omega_{k_z}^{(1,0)}) = \sum_{k_z} \delta(\omega - c\sqrt{(\pi/a)^2 + k_z^2}) = \frac{L}{\pi} \frac{\omega}{c\sqrt{\omega^2 - (c\pi/a)^2}}. \quad (29)$$

For further considering the energy loss caused by the finite conductivity in the waveguide wall, the DOS spectrum can be well fit by taking consideration of the damping factor  $\beta$ . As shown in Supplementary Fig. 1(b), the DOS spectrum is well reproduced by  $D(\omega) = \frac{L}{\pi} \frac{\omega}{c\sqrt{\omega^2 - \omega_{\text{cut}}^2 + i\beta\omega\omega_{\text{cut}}}}$ , with the damping  $\beta$  and propagation distance  $L$  fitted by 0.0159 and 0.03 m, respectively.

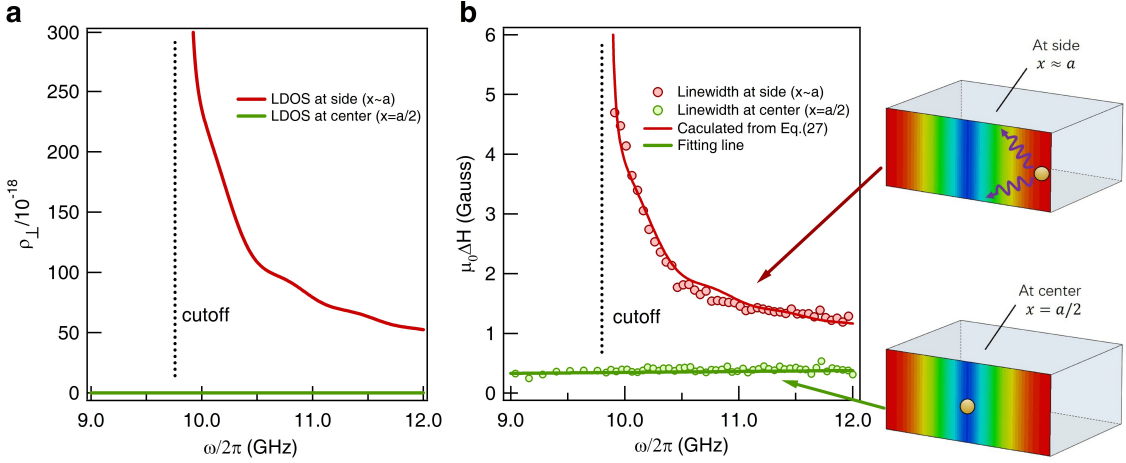
## 2.2 Magnon linewidth enhancement near mode cut-off

In this part, the magnon linewidth enhancement near waveguide cutoff frequency can be directly tested in our standard rectangular waveguide, in which the section is uniform along the waveguide. This allows a direct comparison between the theory [Supplementary Eq. (27)] and experimental observation without the approximation that the section varies slowly along the waveguide.

We introduce a 1 mm highly-polished YIG sphere into the rectangular waveguide to display the damping control via photon states. We place the YIG sphere in two different positions, i.e., at the cross-section center and close to the conductive wall of the waveguide. By fitting the linewidth of  $|S_{21}(H)|^2$  spectra at different microwave frequencies  $\omega$ , we can plot the magnon linewidth  $\mu_0\Delta H$  as a function of  $\omega$  in Supplementary Fig. 2 for two different positions, respectively.

At the cross-section center with  $x = a/2$ , the microwave LDOS is found to be nearly zero [see the green curve in Supplementary Fig. 2(a)] and therefore LDOS-induced radiation damping can be approximately neglected here. As a result, intrinsic magnon linewidth can be obtained from our measurement, with a typical linear  $\Delta H - \omega$  revealed in Supplementary Fig. 2(b) by the green circles. Using linear fitting, the Gilbert damping coefficient can be obtained as  $4.3 \times 10^{-5}$  with the inhomogeneous broadening  $\mu_0\Delta H_0$  fitted by 0.19 Gauss.

As shown in Supplementary Fig. 2(a) by the red curve, LDOS near waveguide wall displays larger magnitude with an obvious enhancement near the mode cut-off frequency. Hence by moving the YIG sphere to near the conductive wall, we expect and indeed obtain a magnon linewidth enhancement according to Supplementary Eq. (27). Specifically, we plot the measured magnon linewidth as a function of frequency in Supplementary Fig. 2 (b) by the red circles. Compared to  $\Delta H - \omega$  relation when YIG is placed at center, here we observe significant magnon linewidth enhancement especially at the frequency near the mode cut-off. Such linewidth broadening can be well reproduced by our calculation from Supplementary Eq. (27) with the fitting parameter  $R$  close to unity.



**Supplementary Figure 2: Magnon radiative linewidth in a rectangular waveguide.** (a) Simulated LDOS  $\rho_{\perp}$  (local density of photon states) when placing YIG (yttrium iron garnet) sphere at waveguide center and near waveguide wall, respectively. (b) Measured magnon linewidth for two different positions with the YIG sphere placed in the center  $x = a/2$  (green dots) and close to conductive wall  $x \sim a$  (red dots). Red solid curve in (b) is calculated from Supplementary Eq. (27) in Supplementary Note 1 and the green solid curve is fitted for intrinsic linewidth. Errors of linewidth fit are smaller than the size of symbols.

## Supplementary References

- [1] Fano, U. Effects of Configuration Interaction on Intensities and Phase Shifts. *Phys. Rev.* **124**, 1866 (1961).
- [2] Mahan, G. D. *Many Particle Physics* (Plenum, New York, 1990).
- [3] Jackson, J. D. *Classical Electrodynamics*, (Wiley, New York, 1998).
- [4] Kittel, C., *Quantum Theory of Solids* (Wiley, New York, 1963).
- [5] Kamra, A. & Belzig, W. Super-Poissonian Shot Noise of Squeezed-Magnon Mediated Spin Transport. *Phys. Rev. Lett.* **116**, 146601 (2016).
- [6] Holstein, T. & Primakoff, H. Field Dependence of the Intrinsic Domain Magnetization of a Ferromagnet. *Phys. Rev.* **58**, 1098 (1940).
- [7] Walker, L. R. Magnetostatic Modes in Ferromagnetic Resonance. *Phys. Rev.* **105**, 390 (1957).
- [8] Verba, R., Melkov, G., Tiberkevich, V. & Slavin, A. Collective spin-wave excitations in a two-dimensional array of coupled magnetic nanodots. *Phys. Rev. B* **85**, 014427 (2012).

- [9] Taflove, A., Oskooi, A. & Johnson, S. G. *Advances in FDTD computational electrodynamics: photonics and Nanotechnology* (Artech house, Norwood, 2013).
- [10] Davy, M., Shi, Z., Wang, J., Cheng, X. & Genack, A. Z. Transmission Eigenchannels and the Densities of States of Random Media. *Phys. Rev. Lett.* **114**, 033901 (2015).
- [11] Genack, A. Z., Sebbah, P., Stoytchev, M., & van Tiggelen, B. A. Statistics of Wave Dynamics in Random Media. *Phys. Rev. Lett.* **82**, 715 (1999).